International Journal of Computer Vision 35:1, pages 65-85, Nov 1998.

International Journal of Computer Vision, ?, 1–23 (????)

Volumetric Deformation Analysis Using Mechanics–Based Data Fusion: Applications in Cardiac Motion Recovery *

PENGCHENG SHI
Department of Diagnostic Radiology, Yale University, New Haven, CT 06520

ALBERT J. SINUSAS
Section of Cardiology, Department of Medicine, Yale University, New Haven, CT 06520

R. TODD CONSTABLE
Department of Diagnostic Radiology, Yale University, New Haven, CT 06520

JAMES S. DUNCAN
Departments of Diagnostic Radiology and Electrical Engineering, Yale University, New Haven, CT 06520

Received ?, ?; Revised ?, ?

Editors: Takeo Kanade and Olivier Faugeras

Abstract. Non–rigid motion estimation from image sequences is essential in analyzing and understanding the dynamic behaviors of physical objects. One important example is the dense field motion analysis of the cardiac wall, which could potentially help to better understand the physiological processes associated with heart disease and to provide improvement in patient diagnosis and treatment. In this paper, we present a new method of estimating volumetric deformation by integrating intrinsic instantaneous velocity data with geometrical token displacement information, based upon continuum mechanics principles. This object–dependent approach allows the incorporation of physically meaningful constraints into the ill–posed motion recovery problem, and the integration of the two disparate but complementary data sources overcomes some of the limitations of the single image source based motion estimation approaches.

Keywords: Nonrigid motion, cardiac motion, continuum model, data fusion, physics-based vision, biomedical image analysis

1. Introduction

Motion and deformation analysis has been of great interest in computer vision research and applications. The goal is to quantitatively extract the temporal kinematic changes, rigid or non–rigid, of the objects depicted in the image sequence. In general, it is a correspondence problem which involves finding the positions of the object points at successive image frames (the motion of each

*This work is supported by Grants No. 2R01HL44803 and No. F32HL09433 of the National Institutes of Health.

International Journal of Computer Vision 35:1, pages 65-85, Nov 1998.

point). It is also a classification problem which deals with measuring motion differences among different object points (the deformation of the object) if non–rigid motion is present. The results are often essential in analyzing the dynamic behavior of many physical objects. While three–dimensional (3D) non–rigid cardiac motion recovery is the focal example of this paper, where the heart translates, rotates, and deforms in 3D space, it is of interest to note that other motion related applications include robot navigation [21], facial recognition [9, 20], articulated motion [25, 47], satellite weather map analysis [52], etc.

1.1. Motion Recovery

Traditionally, the primary emphasis on motion measurement from image sequences has been on the determination of optical flow, a problem long studied in the computer vision literature and which these papers illustrate: Anandan [3], Bajcsy [6], Hildreth [29], Horn [32], Kanade [15], Nagel [44], and Tsotsos [70], etc., as well as medical application oriented works [40, 63]. Although many of these optical flow based methods are based upon solid theoretical foundations, including physical and geometrical models of the object and various coherent constraints on its motion pattern, they are generally not very successful in estimating the true motion field of deformable objects, where non-linear mapping functions are needed to express the point correspondences. One reason seems to arise from the fact that for discrete image sequences, inter-frame displacements are often larger than image resolution, which makes it difficult to use local operations to track the true motion, although multi-resolution or scale-space approaches [8, 16, 75] do offer possible remedy for this particular problem. Also, non–rigid motion makes it more difficult to enforce the smoothness constraints effectively on the optical flow field which are necessary to deal with the aperture problem. Furthermore, as Horn suggested [31], the motion field, defined as the displacement vector field of each point of each object in the image, is usually not exactly the same as the optical flow, the apparent motion of the brightness pattern. It has been demonstrated that the actual correspondence process takes place beyond the level of the raw gray level intensity values [41]. It has also been suggested in Ullman's report that, at least in the human visual system, the edges or the boundaries of the objects are the tokens used in the correspondence process [71], which becomes the foundation of many boundary-based motion tracking algorithms, and was heuristically validated by Slager *et al* [61] in analyzing cardiac image sequence.

Boundary-based motion analysis of non-rigid objects has often been seen as a two step process: first establishing correspondence between certain sub-sampled points of the boundary at time t and time $t + 1$, then using these correspondences as a guide to solve for a complete mapping of the object points between the two time frames. There have been considerable efforts in general on these two topics, although rarely have they been addressed together. While earlier approaches used simple global distance measures to find correspondence, more recent matching methods have been mainly based on tracking salient image features over time, from simple tokens such as points or line segments to complex structures. Curvatures of contour and surface are used for non-rigid bending motion [38, 51, 59], Gaussian curvature is used to estimate point correspondence when the surface is undergoing conformal motion with constant, linear, and polynomial stretching [39], and the principal curvatures are used to recover surface motion under a hybrid bending and stretching model [1]. A somewhat different but certainly interesting approach by Sclaroff and Pentland establishes correspondence by matching shapes in eigen-modal space of a finite element representation of the object in different images [57],and then recover the correspondence in the object space.

The task of establishing a complete non-linear mapping between object frames has received more attention. In all of these approaches, estimates of correspondence between sparse individual points on objects are either specifically assumed to be known or established based on some global distance measures. Metaxas and Terzopoulos have advocated general global parameterized deformable superquadrics that can be locally deformed or modified [17, 67]. Physically-based finite element models are used by Pentland [33] and Ayache [45] to provide a framework for the mappings, and modal analysis is adopted to re-

International Journal of Computer Vision 35:1, pages 65-85, Nov 1998.

duce computational cost. Other finite element mesh-based approaches have introduced flexible adaptive-size models [68]. Bookstein [11] used deformable thin-plate spline models to interpolate dense correspondence from very sparse initial matches. To certain extent, our proposed approach is following this physically-motivated paradigm. However, we try to employ truly physically meaningful constraints, instead of merely physically motivated models, on the dynamic behaviors of the object, which enable us to incorporate naturally actual known physical parameters into the motion estimation framework.

1.2. Cardiac Deformation Analysis

Accurate estimation of cardiac deformation has long been an interesting and important study case for non-rigid motion recovery [1, 39, 45, 54, 33, 59, 58]. The complexity of the myocardial motion and the absence of internal landmarks imply that the true motion characteristics of heart tissue elements are, at best, difficult to infer from sequential images. In addition, it is not only a challenging computer vision problem, but is also essential in evaluating the cardiac physiological and pathological conditions to detect ischemic heart disease. The ability to make cardiac motion measurements has a variety of benefits, including that image-based serial analysis of regional function is helpful in assessing the efficacy of therapeutic agents as well as mechanical interventions [13, 26].

In addition to the above mentioned general non-rigid motion algorithms which have been or could be applied in cardiac image analysis, there are active efforts in medical image analysis community that are more specifically aimed at heart motion estimation. Several approaches attempt to detect optical flow of cardiac image sequences [40, 63, 69]. Other approaches try to track the movement of the pre-extracted boundary points of the cardiac wall, where geometric tokens are used as tracking cues [10, 23, 39, 38, 51]. The use of identifiable shape information seems to be supported by an important validation study in two-dimensional (2D) image sequences by Slager *et al* [61]. Some of these boundary-based methods suffer from using only the end-diastolic (ED) and end-systolic (ES) image frames while ignoring the important temporal evolution of the motion pattern [24], some others have been hampered by relying on 2D image sequence data. The 3D nature of the cardiac motion means that measurements from 2D image sequences most likely are not made from the same points on the cardiac boundaries at different time instants, and hence do not track the true movement of the heart.

Interestingly, there have been several very impressive development in medical imaging community to produce better and information-richer image data on cardiac motion. In magnetic resonance tagging, a spatially varying pattern of magnetization is encoded into the myocardium prior to each phase-encoded data acquisition cycle of a spin-echo imaging sequence, forming a grid pattern of image voids [4, 78]. Motion that occurs between the time the tags are laid down and a later point in time results in a distortion of the tag pattern which can be tracked over a portion of the cardiac cycle. In order to obtain data pertaining to deformation in three dimensions, 2D tag data must be acquired in two orthogonal views [5]. It is important to notice that the same tissue elements are not tagged in each of the two views, thus the deformation in each view must be seen as partial 2D data at different points that contributes to an overall scheme aimed at estimating the complete 3D motion and deformation. A variety of approaches have been designed to estimate motion from tagging images. Several of the most relevant ideas are the finite element models that incorporate spring-like interconnections and nonlinear basis functions [77], locally deformable superquadrics [54], B-snake interpolation [2], high order polynomial fitting of the sparse tag points [49], and an estimation theory based idea which uses a stochastic vector field to assist in the interpolation [18].

Another new medical imaging data is the so-called phase contrast MR imaging. The physics basis is that a uniform motion of tissue in the presence of a magnetic field gradient produces a change in the MR signal phase which is proportional to its velocity. In addition, the velocity in any particular spatial direction can be estimated by measuring the difference in phase shift between two acquisitions with different first gradient moments [46]. Currently, phase contrast velocity estimates near the cardiac wall boundaries are quite

International Journal of Computer Vision 35:1, pages 65-85, Nov 1998.

noisy because spatial averaging must occur. In addition, since the velocity maps themselves do not establish the point correspondences between image frames, methods need to be devised to accurately track each segment of myocardium as it deforms through the cardiac cycle. Approaches that use forward, backward, or combined forward and backward, integration of the velocity to estimate the displacement vector have been proposed [14, 28, 55, 74]. In addition, Meyer [43] suggests a framework which combines a spatially regularizing velocity field with temporal Kalman filtering to characterize the deforming LV in 2D.

1.3. Possible New Directions In Cardiac Motion

One observation stems from the importance of volumetric analysis of heart motion. The assessment of degree of transmural injury is one critical aspect of evaluating the mechanical performance of myocardial dynamics in general, and patient prognosis in particular. A complete appreciation of the image analysis results only occurs from volumetric data. While current approaches have attacked some aspects of cardiac motion recovery problem from different angles, they have mostly concentrated on either boundary information or mid-wall but not both, which makes them inherently use incomplete information. In addition, even though there are approaches utilizing the new medical imaging data, there has been no work attempting to merge complementary computer vision based matching strategies with imaging physics based concepts within a unified framework. One possible reason is the fact that an appropriate computational framework has not yet been developed for assembling various complex cues related to cardiac deformation that are available from image data sets.

Another observation rises from the very active research in the biomechanics community that is aimed at deriving quantitative descriptions of local myocardial motion and material characteristics, including the distributions of stress and strain, the local tissue properties represented by constitutive relationships, etc. [27, 30, 37, 48, 72, 76]. These local quantities are particular important in understanding the mechanics of pathological conditions such as myocardial ischemia and hypertrophy, and they are also invaluable for mathematical and computational modeling of the beating heart. While in physics-based computer vision research, efforts have been made to use simple, generic, and empirical physical principles to achieve local smoothness and data-driven interpolation, there have been little use of known, true physical constraints pertaining to the objects we are studying. For biological objects with complex behavior such as the heart, any additional information will certainly help to more accurately derive useful results from the images. It is our assertion that the use of true mechanical models as a means to guide image understanding is an attractive new direction for certain image analysis problems, especially with regards to biological objects. For the purposes of heart motion estimation, we are particular interested in computationally accessible ideas that focus on the solid mechanics modeling of the myocardium which are suitable to be integrated with our image-derived recovery.

1.4. Proposed Approach

We propose here an integrated framework for the analysis of three-dimensional motion and deformation of the heart. This unified approach is based upon the use of image analysis strategies and biomechanical modeling of the myocardial tissue, and is embedded in a finite element framework for the integration of disparate sources of displacement and velocity information, heretobefore used only separately, to help guide volumetric motion and deformation analysis. In this manner, noisy and complementary image information can be jointly utilized from both the heart wall boundaries (where the shape-based estimated displacements are reliable) and the mid-wall (where measures such as MR phase velocity, MR tagging, and echocardiographic Doppler are reliable). In addition, the continuum mechanical properties of the myocardium provide physically meaningful constraints on the dynamic behaviors of the myocardial tissue. This, along with the finite element framework, enable us to incorporate naturally actual known cardiac physical parameters, such as pressures, into the motion/deformation estimation system.

International Journal of Computer Vision 35:1, pages 65-85, Nov 1998.

While the framework presented here is currently aimed at cardiac motion analysis, we believe that it has at least two aspects which can be applied in certain areas of computer vision research in general. One is the use of true physical properties of the objects to incorporate more meaningful constraints, in place of empirical geometrical or physically-motivated models. The other is the integration of complementary image-derived data, a mechanics-based fusion in our example, to achieve more robust results.

2. Image–Derived Information

It is the aim of the proposed motion and deformation analysis framework to more completely characterize the transmural function of the left ventricle (LV). Towards this goal, we believe that integration of several complementary image sources of LV anatomy and motion provides a more robust way for quantifying the dynamic behavior of the myocardium. In this section, we will briefly discuss several of the image-derived sources of data which have been used in our framework.

2.1. Shape–Based Boundary Displacement

We have previously proposed that we can use the shape properties of the endocardial and epicardial surfaces to track the motion of a dense field of LV surface points over the entire cardiac cycle [59]. Here, we assume that the myocardium boundaries have been segmented [12, 65], and we only deal with boundary surface points. Our motion tracking method is based on locating and matching differential geometric surface landmarks and using a mathematical optimization reasoning strategy to combine a locally coherent smoothness model with data-derived information to obtain dense field motion vectors. Favorable tracking results validated by implanted physical markers have been observed [59].

2.1.1. Surface Representation Since the motion tracking strategy is based upon the boundary shape characteristics, a good surface representation is needed to infer the geometrical parameters of the LV surfaces. Delaunay triangulation is most suitable for volumetric representation of spatial point set without *a priori* connectivity information, and it defines a symmetrical and isotropic neighborhood point relationship. For any 3D point set, the Delaunay triangulation [73] defines a simplex decomposition of the convex hull of the point set, where the vertices of all tetrahedra are contained in the point set. Its most important property is that the circumsphere of every tetrahedron contains no other point from the point set, which can be used to prove that the Delaunay triangulation is a globally optimal triangulation in the sense that the tetrahedra are as *regular* as possible. An algorithm based on incremental point insertion into a pre–existing Delaunay triangulation [73] is implemented, which is of $O(N^2)$ in the worst case. For the myocardial boundary point set, the two-dimensional Delaunay facets which are on the boundary of a bounded and constrained Delaunay triangulation constitute the LV endocardial and epicardial surfaces [60]. Figure 1 shows the Delaunay tessellated endocardial and epicardial surfaces from an MRI dataset.

2.1.2. Surface Shape Characteristics To be able to analyze the local shape properties around a point p in a neighborhood of a triangulated surface S, the trace of the polynomial is used to approximate this neighborhood in the form of the graph of a differentiable function. We choose the local coordinate system in such a way that the origin O is at p and the z axis is directed along the outward normal at p (thus, the xy plane agrees with the tangent plane $T_p(S)$). It follows that a neighborhood of p in S can be represented in the form $z = h(x, y)$, where h is a differentiable function, with $h(0,0) = 0, h_x(0,0) = 0, h_y(0,0) = 0$. In order to choose a neighborhood of p which is unique (no folding) and local (no non-neighboring points) under the local coordinates, the natural neighbor relationship between surface points should be used to define a precise and flexible neighborhood [60].

Since the Weingarten mapping matrix only depends on the first and second derivatives of the graph function $h(x, y)$, biquadratic functions are all we need to estimate the curvatures of the local surface, assuming that the local surfaces are well behaved such that a biquadratic polynomial can approximate a patch sufficiently closely. The estimate of the biquadratic graph function involves

International Journal of Computer Vision 35:1, pages 65-85, Nov 1998.

finding the five coefficients of the polynomial:

$$z = h(x, y) = a_1x^2 + a_2xy + a_3y^2 + a_4x + a_5y \quad (1)$$

If there are at least four neighboring points, say $n - 1 (n \geq 5)$ points, the least-square estimate of the five coefficients is evident. Once the coefficients are found, computing the actual differential properties on the fiducial point is straightforward [19].

Since the surface curvatures are the only natural algebraic invariants of the Weingarten mapping matrix, they arise naturally in a detailed analysis of surface shape. Gaussian and mean curvatures are invariant to arbitrary choice of local parameterization of a surface patch, and are also invariant to arbitrary rotations and translations of the surface patch in space. These invariances are extremely important in uniquely characterizing the view-independent surface shape properties. The analysis of the left ventricular surfaces is based upon these invariances for characterizing their shape properties. The principal curvatures, the two eigenvalues of the Weingarten mapping matrix, provide an equivalent description of the local surface shape. Moreover, they also provide the directional information of the surface shape, which could be important in finding certain higher order differential features of the surface, such as ridge lines. Figure 2 shows the curvature maps of an endocardial and an epicardial surface at one time point.

2.1.3. Surface Motion Tracking The movement of a set of LV surface points over the cardiac cycle is determined by following local surface shape between successive surface frames. First, the myocardial surface at one given time instant is subsampled to create a sparser set of points (the experimental results shown later are obtained using a ten percent sampling rate) in order to avoid cross-overs between local matches. Under the assumption that the LV surface deforms as little as possible between small time intervals, the sub-sampled surface points are matched and followed over the LV surface sequence under a minimum bending energy model. Then, match-confidence-weighted regularization functionals are constructed to compute the dense field motion for all the surface points.

Shape-Based Initial Matching. Local surface patches on the LV are modeled as thin flexible plates, loosely constrained to deform in a predetermined fashion. The potential energy of an ideal thin flexible plate of elastic material is a measure of the strain energy of the deformation:

$$\epsilon_{be} = A\Big(\frac{(\kappa_1 - \bar{\kappa}_1)^2 + (\kappa_2 - \bar{\kappa}_2)^2}{2}\Big) \quad (2)$$

The principal curvatures of the initial surface patch are κ_1 and κ_2, while the same parameters of the deformed surface patch are $\bar{\kappa}_1$ and $\bar{\kappa}_2$, and A is material specific constant. This equation arrives at a numerical value measuring the energy required to deform the initial surface patch to achieve a deformed shape. Obviously, if the surface patch undergoes rigid motion, there is no bending energy required for the movement since the shape of the patch does not change. Only non-rigid deformation requires bending energy, which is a form of strain energy.

Under the assumption that the surface patch surrounding each sample point $\mathbf{x}$ deforms only slightly and locally within a small time interval, we construct a physically-plausible search region W on the second surface at time t_{i+1} for each sampled point on the first surface at time t_i. Surface points inside W constitute the candidate point set $\{\mathbf{x}_{W,i}, i = 0, ..., N-1\}$. Bending energy measures between the surface patch surrounding point $\mathbf{x}$ and surface patches surrounding candidate points $\mathbf{x}_{W,i}$ are computed, and the point $\bar{\mathbf{x}}$ that has the *minimum* corresponding bending energy is chosen as the point corresponding to point $\mathbf{x}$.:

$$\begin{aligned} \bar{\mathbf{x}} &= \arg\min_{\mathbf{x}_{W,i}} \epsilon_{be}(\mathbf{x}, \mathbf{x}_{W,i}) \\ &= \arg\min_{\mathbf{x}_{W,i}} A\Big(\frac{(\kappa_1(\mathbf{x}) - \kappa_1(\mathbf{x}_{W,i}))^2}{2} \\ &\quad + \frac{(\kappa_2(\mathbf{x}) - \kappa_2(\mathbf{x}_{W,i}))^2}{2}\Big) \end{aligned} \quad (3)$$

Repeating the matching process for all the sub-sampled points of the surface at t_i, the results yield a set of sparse, shape-based, best-matched motion vectors $\mathbf{d}_{init}(\mathbf{x}, t_i) = \bar{\mathbf{x}} - \mathbf{x}$ for pairs of surfaces derived from 3D image sequences. An example of bending energy-based matching of an endocardial surface point is shown in Figure 3.

International Journal of Computer Vision 35:1, pages 65-85, Nov 1998.

Confidence Measures. The bending energy measures for all the points inside each search window are also recorded as the basis to measure the *goodness* and *uniqueness* of the matching choices. The value of the minimum bending energy in the search region between the matched points indicates the goodness of the match:

$$m_g(\mathbf{x}) = \epsilon_{be}(\mathbf{x}, \bar{\mathbf{x}}) \tag{4}$$

Meanwhile, it is also desirable that the chosen matching point is a unique choice among the candidate points within the search window, which means that ideally the bending energy value of the chosen point should be much smaller than those of the rest of the points. We denote the mean values of the bending energy measures of all the points inside window W except the chosen point as $\bar{\epsilon}_{be}$ and their standard deviation as σ_{be}, we define the uniqueness measure as:

$$m_u(\mathbf{x}) = \frac{\epsilon_{be}(\mathbf{x}, \bar{\mathbf{x}})}{\bar{\epsilon}_{be} - \sigma_{be}} \tag{5}$$

This uniqueness measure means that if the bending energy of the chosen point is small compared to some window-specific value of the remaining bending energy measures (mean minus standard deviation), it is quite unique and reliable, otherwise it is not. Obviously for both goodness and unique measures, the smaller the values the more reliable the match are. Combining these two measures together, we arrive at one *confidence measure* for the matched point $\bar{\mathbf{x}}$ of point $\mathbf{x}$:

$$c(\mathbf{x}) = \frac{1}{k_{1,g} + k_{2,g} m_g(\mathbf{x})} \; \frac{1}{k_{1,u} + k_{2,u} m_u(\mathbf{x})} \tag{6}$$

where $k_{1,g}, k_{2,g}, k_{1,u}$, and $k_{2,u}$ are scaling constants for normalization purposes. The confidence measures for all the surface matches are normalized to the range of 0 to 1. The matches with the highest confidence have the confidence measure value of 1, and the matches with the lowest confidence have the confidence measure value of 0.

The above derived confidence measure represents our empirical notions of goodness and uniqueness. While it has worked fine in our experiment of about twenty datasets, further efforts are needed to formalize and test statistically or physically more meaningful confidence measures.

Optimized Dense Motion Field. Based upon the physically-plausible assumption that the displacement fields of the LV surfaces are sufficiently smooth and that any changes of direction and magnitude take place in a gradual manner over space, a regularizing functional which includes both an initial estimate adherence term and a local smoothness term is constructed. Since the reliability of the initial correspondences vary based on their confidence measures, it should be clear that good, unique matches from the initial bending energy matching process should be preserved, while ambiguous matches should be smoothed over by their neighboring good and unique matches.

In the continuous domain, the regularizing smoothing function is constructed as

$$\begin{aligned} \mathbf{d}^*(\mathbf{x}) \;=\; & \arg\min_{\mathbf{d}} \int\int_S \{c(\mathbf{x})[\mathbf{d}(\mathbf{x}) - \mathbf{d}_{init}(\mathbf{x})]^2 \\ & + (\frac{\partial \mathbf{d}(\mathbf{x})}{\partial \mathbf{x}})^2\} d\mathbf{x} \end{aligned} \tag{7}$$

Here, S is the surface space, $\mathbf{x}$ is the parameter vector representing a point in S, $\mathbf{d}_{init}$ and $\mathbf{d}^*$ are the initial and final displacement vectors, respectively, and $c(\mathbf{x})$ is the confidence measure.

Since we are dealing with discrete polyhedral surfaces, the derivative of the displacement vector can be approximated by the weighted average finite differences performed on the neighboring points. Furthermore, the discrete version of the smoothing function can be conveniently posed as a series of linear equations, and can be solved by a two-stage iterative procedure which will avoid the shrinkage problem often hinder the regular one-step smoothing [66]:

$$\begin{aligned} \mathbf{d}(\mathbf{x})_{new1} \;=\; & (1 - c_1'(\mathbf{x}))\mathbf{d}(\mathbf{x})_{old} \\ & + c_1'(\mathbf{x}) \sum_{i=0}^{N-1} \omega_i \mathbf{d}(\mathbf{x}_i) \end{aligned} \tag{8}$$

$$\begin{aligned} \mathbf{d}(\mathbf{x})_{new2} \;=\; & (1 - c_2'(\mathbf{x}))\mathbf{d}(\mathbf{x})_{new1} \\ & + c_2'(\mathbf{x}) \sum_{i=0}^{N-1} \omega_i \mathbf{d}(\mathbf{x}_i) \end{aligned} \tag{9}$$

where $\{\omega_i\}$ is the weighting coefficient set associated with the neighbor points, and c_1', c_2' are derived from the confidence measure c [59].

The solution of this system of linear equations will yield a dense set of smoothed motion vec-

International Journal of Computer Vision 35:1, pages 65-85, Nov 1998.

tors that adhere to the reliable initial shape-based matches, yet vary smoothly on the surface space. Repeating the process for all the LV wall surfaces and assembling the vectors end-to-end over the sixteen-frame temporal sequence, we have a dense set of motion trajectories of the myocardial surface points throughout the cardiac cycle. Figure 4 shows the dense endocardial displacement vector field of a MRI dataset from ED to ES, subsampled for visualization purposes. The trajectories are shown against the rendered endocardial surface at ES.

Extensive validation has been conducted on this shape-based LV surface motion tracking approach. Algorithm-derived motion trajectories of four endocardial and four epicardial points are compared to corresponding implanted imaging opaque makers for twenty image datasets of two imaging modalities. Overall performance has been vert favorable, with average position errors within image resolutions. Please see [59] for more details.

We will use these boundary displacement vectors as the shape-derived boundary information in our integrated framework. For computational stability and for not over constraining the boundary motion by shape information, however, only a subset of boundary displacement vectors in which we have the highest confidence will be used in the integrated estimation process. This subset of boundary displacement vectors is denoted as $\mathbf{U}_{boundary}$.

2.2. MR Phase Contrast Images and Mid-Wall Instantaneous Velocity

As briefly discussed in Section 1, phase velocity magnetic resonance imaging incorporates velocity phase encoding into a conventional cine-MR sequence and produces images of myocardial instantaneous velocity throughout the cardiac cycle. Phase contrast methods can depict motion parameters with pixel precision and thus provide a high resolution technique for quantitative measurements [14].

The MR phase contrast velocity technique relies on the fact that a uniform motion of tissue in the presence of a magnetic field gradient produces a change in the MR signal phase, ϕ, that is proportional to its velocity [56]:

$$\phi = \nu\gamma M_1 = \nu\gamma \int_0^{TE} G(t)t \; dt \qquad (10)$$

where $G(t)$ is the gradient strength as a function of time (the gradient waveform), ν the tissue velocity, M_1 the first moment of the gradient waveform, TE the echo delay time, and γ the gyromagnetic ratio. The gradient waveform can be modified to alter the first moment (motion sensitivity) while maintaining the same image localization characteristics. Images acquired with this altered waveform will have a different phase shift due to motion. The velocity in a particular spatial direction can be estimated by measuring the difference in phase shift between two acquisitions with different first gradient moments. Hence, instantaneous velocity maps encoded for motion in all three spatial dimensions may easily be obtained at multiple time instances throughout the cardiac cycle using a phase contrast cine-MR imaging sequence. The acquired velocity maps may then be used to provide information on tissue displacement, strain, strain rate, and other quantitative measures of motion and deformation. Figure 5 shows examples of phase contrast images of a canine mid-ventricle slice. In this dataset, three contiguous short axis slices were collected using the cine phase contrast gradient echo sequence. It is important to note that the magnitude image and the three directional velocity images are perfectly registered since they are acquired from the same complex MR signal.

In theory, instantaneous velocity can be derived for each pixel in each image acquisition to provide a complete description of instantaneous movement of the LV at that moment. However, the phase contrast velocity estimates at interfaces between structures, e.g. near the endocardial and epicardial boundaries, are extremely noisy [43]. It is difficult to obtain low noise estimates of velocity at the boundaries since some spatial averaging must occur, and thus pixels outside the myocardial wall (the blood pool for the endocardium and the air or other tissues for the epicardium) are sometimes included for the velocity estimates of the myocardial points. Thus, phase contrast images only provide reliable instantaneous motion information for the mid-wall region of the LV but not at the myocardial boundaries.

International Journal of Computer Vision 35:1, pages 65-85, Nov 1998.

We believe that the weaknesses of the phase velocity image data, such as noisy boundary data and uncertainty about point correspondences (currently, constant velocity conditions between temporal frames are often assumed to compute displacements), makes it very difficult to obtain a reliable and robust assessment of myocardial motion and deformation over the entire LV and through the cardiac cycle using these data alone. It is more appropriate to use phase velocity information as one source of data constraints within an integration framework, where it can be utilized without gross assumptions about the velocity conditions between temporal frames. Furthermore, since the phase image is derived from the same complex magnetic resonance signal as the regular magnitude MR image data upon which the shape-based boundary motion algorithm is based, these two sets of image data are perfectly registered and can be used synergistically. Hence, we will use the reliable mid-wall MR phase velocity data as the mid-wall image information in our integrated framework, and we denote these mid-wall velocity vectors as $\dot{\mathbf{U}}_{mid-wall}$.

3. A Mechanics-Based Data Fusion Framework

In this section, we present a new method of estimating left ventricular deformation which integrates instantaneous velocity information from the phase contrast magnetic resonance images within the mid–wall region with the shape-based displacement information on the boundaries of the left ventricle. The integration takes place within a continuum mechanical model of the left ventricle, which is embedded in a finite element analysis framework.

3.1. Continuum Mechanical Model of the Left Ventricle

Here, we discuss some of the basic concepts of continuum mechanics [22, 64] and the modeling of myocardium based on biomechanics research efforts [35, 36, 42, 48, 62]. Detailed discussion can be found in the cited references. It should be pointed out that our emphasis is on using practical yet realistic mechanical models that could be used to guide the recovery of the non-rigid motion of single-body deformable objects.

3.1.1. Continuum Mechanics Continuum mechanics deals with the mechanical behaviors of object under the action of applied force, where the materials are continuous (or at least piecewise continuous) and deformable. The results of applying forces are often found in the changes of the kinematic variables such as displacement, velocity and acceleration fields of the object.

In 3D, an object point is distinguished by its *material coordinates* $\mathbf{X} = (X_1, X_2, X_3)$ at the undeformed state ($t = 0$), while its corresponding coordinates $\mathbf{x} = (x_1, x_2, x_3)$ at the deformed state is called its *spatial coordinates*. The deformation gradient tensor $\mathbf{F}$ relates the deformed and undeformed state by

$$F_{iR} = \frac{\partial x_i}{\partial X_R} \quad i, R = 1, 2, 3. \tag{11}$$

Further, the Lagrangian strain tensor $\mathbf{E}$ is defined as :

$$\mathbf{E} = \frac{1}{2}(\mathbf{F}^T\mathbf{F} - \mathbf{I}) \tag{12}$$

where $\mathbf{I}$ is identity matrix. This is a suitable measure of deformation since it reduces to the zero tensor when there is only rigid-body motion.

However, the strain measure is insufficient to describe the *mechanical behavior* of any particular object, which means that by itself it cannot determine the changes of kinematic variables when forces are applied, or determine the changes of stress when strain is induced. Following the law of conservation of energy, the material time derivative of the sum of the kinetic energy and internal energy is equal to the sum of the rate at which mechanical work is done by the body and surface forces acting on the object and the rate at which other energy (heat flux, chemical energy, radiation energy, electro-magnetic energy, *et al*) enters the object [64]. If other energy is absent or neglected, then all the mechanical work done on an object either creates kinetic energy, or is stored as *strain energy* W which depends only on the deformation. For a general finite elastic deformation of an unknown material, W depends in an *arbitrary* manner on the deformation gradient $\mathbf{F}$. However, the specific manner of this dependence determines the mechanical behavior of any specific material.

International Journal of Computer Vision 35:1, pages 65-85, Nov 1998.

In general, the constitutive equations for a finite elastic solid are defined as:

$$T_{i,j} = \frac{\rho}{\rho_0} F_{jR} \frac{\partial W(\mathbf{F})}{\partial F_{iR}} \quad i,j,R = 1,2,3. \tag{13}$$

where $\mathbf{T}$ is the stress tensor, ρ_0 and ρ the initial and final material density respectively. The equation's apparent simplicity is deceptive, because W is a function of the nine components of $\mathbf{F}$, which makes it impractical to perform experiments to determine this function for any particular elastic material. In practice, various assumptions under different conditions have been made to derive practical yet realistic strain energy functions of the materials, from which the material constitutive laws can be derived.

Since the material constitutive law characterizes the kinematic effects on an object when forces are applied, it represents a true physical model of the object, as least from mechanics point of view. Because of the continuum nature of this type of model, smoothness and other desirable physical and geometrical properties in computer vision are implicitly guaranteed if we use this type of mechanical model. Actually, it can be shown that almost all the geometrical and empirical physical models in computer vision research are equivalent to some forms of simplified constitutive laws, but they may not be in the mechanically plausible manners to preserve the most basic and important material properties of the object [53]. Hence, we believe that using realistic yet computationally plausible constitutive models are essential in deriving *correct* results from image analysis.

3.2. Models of the Myocardium

The mechanical behavior of the myocardium is very diverse and complex, and it would be an admirable but extremely difficult goal to formulate its constitutive equations under all circumstances. Rather, for our purposes, we seek to establish equations which describe the most important features of the material while retaining physical and computational plausibility. Ideally, the constitutive equations of the myocardium should characterize the non-linear, anisotropic material properties of the cardiac muscle in a compact way with as few parameters as possible. The relationship should also be formulated based on experimental measurements.

There has been a fair amount of active research in the biomechanics community in developing myocardial constitutive laws under different conditions and assumptions [35, 36, 42, 48, 62]. In general, two aspects of the mechanical properties of the myocardium have been considered: the passive tissue properties and the active muscle tension development. A constitutive law for passive tissue properties requires a fully three-dimensional relationship between the six components of the stress and the six components of the strain (assuming symmetric material), whereas the active muscle law requires only a one-dimensional relationship between the fiber strain and the active muscle tension in the myofiber direction [36]. Since the purpose of our system is to use the constitutive relationship to help recover motion and deformation from image data, not to model the forward activation of the left ventricle, we have focused on the passive constitutive laws. However, we do realize that the active muscle tension development largely determines the active contraction and expansion of the myocardium, and incorporating active muscle law into our framework would add important actual physical constraints into the recovery process.

The simplest constitutive relationship is that of the linear (*Hookean*) elastic solid under infinitesimal deformation, where the strain energy function has the form

$$W = \frac{1}{2} c_{ijkl} \epsilon_{ij} \epsilon_{kl} \tag{14}$$

Here, ϵ_{ij} and ϵ_{kl} are components of the infinitesimal strain tensor and c_{ijkl} are material specific elastic constants. Under this model, the constitutive equation can be simplified to:

$$\sigma_{ij} = c_{ijkl} \epsilon_{kl} \tag{15}$$

where σ_{ij} is a stress tensor component. It is evident that the stress components are linear functions of the infinitesimal strain components. Under the assumptions that the strain and stress tensors are symmetric, and the material is isotropic (the elastic properties are identical in all directions), there are exactly two elastic constants which characterize the material and the constitu-

International Journal of Computer Vision 35:1, pages 65-85, Nov 1998.

tive equation is further reduced to:

$$\sigma_{ij} = \lambda\delta_{ij}\epsilon_{kk} + 2\mu\epsilon_{ij} \tag{16}$$

where constants λ and μ are the so called *Lame constants*. Further, the familiar material constants *Young's modulus* $E = \frac{\mu(3\lambda+2\mu)}{\lambda+\mu}$ and the *Poisson's ratio* $\nu = \frac{\lambda}{2(\lambda+\mu)}$ can be derived. It should be noted that these linear, isotropic constitutive equations *do not* properly describe the mechanical behaviors of the myocardium because myocardium is non-linear and anisotropic material undergoing finite deformation. However, they are very simple to use in a computational framework, and are often treated as the first order approximations of more sophisticated constitutive laws under small deformation conditions.

More sophisticated models of the myocardium often take into account the micro-structures of the cardiac muscle. The architectures and orientations of the myofibers, the organization of the myocardial sheets, and the collagen inter-connections between the micro-structures determine the non-homogeneous and non-linear stress-strain relationship throughout the myocardium [36, 42]. Because the composition of the myocardial tissue is often too complex to derive constitutive laws from the knowledge of the mechanical properties and layout of the micro-structural components, simpler empirical relationships were proposed and constitutive parameters estimated from biaxial testing of the tissue were used [35, 48, 62]. While such non-linear models more appropriately describe the complex mechanical properties of the myocardium, they are often computationally very expensive.

In this paper, all the experiments have been conducted using the linear isotropic model, which is more computationally feasible. However, the different choices for the continuum models of the myocardium *do not* change the fundamental underlying concepts of the integrated framework to recover motion and deformation from image data, although we do realize that more sophisticated non-linear models probably will produce more realistic and accurate results. And we are in the process of implementing more realistic models [53].

3.3. Finite Element Representation

The finite element method (FEM) is a numerical analysis technique for obtaining approximate solutions to a wide variety of engineering problems, especially continuum mechanics problems [7]. Its basic premise is that a solution region can be analytically modeled or approximated by replacing it with an assemblage of discrete finite elements, and by expressing the unknown field variable in terms of assumed approximating or interpolation functions within each element. In essence, a complex problem over a large solution region can be reduced to a series of greatly simplified problems over many finite elements, and the solutions to a series of governing equations of the elements give a piecewise approximation to the solution of the governing equation of the original system [34]. For our framework of left ventricular motion and deformation analysis, the LV (the solution region) is represented by many small tetrahedra (the finite elements) constructed from the Delaunay triangulation of the sampled points. Also, the displacement-based solutions of the governing equations give the approximate motion at the sampled points and the deformation of the elements.

We derive the governing equations of the dynamics of the three-dimensional myocardium using the minimum potential energy principle, based on an isotropic linear elastic model. If $\Pi(u, v, w)$ is the potential energy, $U_p(u, v, w)$ is the strain energy, and $V_p(u, v, w)$ is the work done by the applied loads during the displacement changes, then we have at equilibrium (by neglecting other energy terms such as heat)

$$\begin{aligned} \delta\Pi(u, w, v) &= \delta[U_p(u, v, w) - V_p(u, v, w)] \\ &= 0 \end{aligned} \tag{17}$$

In this case, the strain energy is solely a function of the strain and stress tensors, and can be expressed as:

$$U_p(u, v, w) = \frac{1}{2}\int\int\int_{\Omega} [\epsilon]^T[\sigma]dV \tag{18}$$

where Ω is the volume of the body. The work done by the external forces, including the body forces $[R_b]$, the surface traction $[R_s]$ and the con-

International Journal of Computer Vision 35:1, pages 65-85, Nov 1998.

centrated forces $[R_i]$, is given by:

$$\begin{aligned} V_p(u,v,w) &= \int\int\int_\Omega [\mathbf{U}]^T[R_b]\ dV \\ &+ \int\int_S [\mathbf{U}]^T[R_s]\ dS \\ &+ \sum_i [\mathbf{U}]^T[R_i] \end{aligned} \tag{19}$$

For the left ventricle, the body forces $[R_b]$ are mostly gravitational which are from the myocardium density, surface traction $[R_s]$ and concentrated forces $[R_i]$ include forces arising from the ventricular blood pressure on the endocardium (often available) and the reaction forces from the adjoining structures such as the lung (difficult to measure). The displacement field $\mathbf{U}$ (congregate of all the 3D displacement vectors of the myocardial points) that minimize Π and satisfies all the boundary conditions is the equilibrium displacement.

Assume that the volume Ω of the linear elastic body is divided into M discrete elements. We may write the potential energy of the body (the assemblage of the elements) as the sum of the potential energies of all elements, and we may deal with the potential energy of an isolated element e and arrive at the governing equilibrium equation for element e

$$\begin{aligned} &[M]^{(e)}[\ddot{\mathbf{U}}]^{(e)} + [C]^{(e)}[\dot{\mathbf{U}}]^{(e)} + [K]^{(e)}[\mathbf{U}]^{(e)} \\ &= [R]^{(e)} \end{aligned} \tag{20}$$

where $[M]^{(e)}$ is the mass matrix of the element, $[C]^{(e)}$ the damping matrix, $[K]^{(e)}$ the stiffness matrix, $[R]^{(e)}$ the force vector, and $[\mathbf{U}]^{(e)}$ the displacement field of element e.

It is worth to pointing out that even though the element matrices $[M]^{(e)}$, $[C]^{(e)}$, and $[K]^{(e)}$ for any element e all take the same forms, the actual terms of the mass, damping, and stiffness matrices can vary even among elements with the *same geometry and same interpolation functions*. This is because different elements can have different material constitutive laws, different material densities, and different damping characteristics. This non-homogeneity gives us the flexibility to model different regions of the left ventricle differently, based upon any prior knowledge about the tissue. To a certain degree, it also justifies the choice of the computationally efficient linear elastic model because each small piece of tissue can always be approximated to be a linear isotropic elastic material if the size and the deformation of the element are small enough.

After the governing equilibrium equations of all the elements have been found, the next step in the finite element analysis of the left ventricle is to combine all these equations to form a complete set of system equations which govern the composite of elements. The system assembly procedure is based on the insistence of *compatibility* at the element nodes. By this we mean that at any node where elements are connected the values of the unknown nodal variables (displacement) are the same for all elements connecting at that node. When these displacements are matched at the nodes, the nodal stiffness, mass, damping, and loads for each of the elements sharing the node are added together to obtain the net stiffness, mass, damping, and loads at that node:

$$[M][\ddot{\mathbf{U}}] + [C][\dot{\mathbf{U}}] + [K][\mathbf{U}] = [R] \tag{21}$$

where $[\mathbf{U}]$ the nodal displacement vector field for the entire body. It should be noted that while the finite element mesh provides the basis for approximating a continuous spatial model of the left ventricle, the governing equations provide the basis of an appropriate temporal model for the motion and deformation analysis.

3.4. Our Approach: Integrated Motion Analysis

Following the procedures described above, we have developed a finite element framework of the left ventricle, modeled by linear isotropic elastic material, and we can use this system to pursue the integrated approach of quantifying LV motion and deformation. Complementary image derived information are incorporated into the framework to recover the volumetric deformation. For the remainder of this paper, we will assume that the image-based sources include boundary constraints (shape-based displacements), computed from segmented MR magnitude images, and mid-wall constraints (instantaneous phase velocity) from corresponding MR phase contrast images. We should also point out that we are analyzing frame-to-frame motion and deformation, which means that the framework only attempts to quantify the LV

International Journal of Computer Vision 35:1, pages 65-85, Nov 1998.

tissue movement between pairs of temporally consecutive image frames. Even though we do analyze motion and deformation for all sixteen pairs of image frames, and changes between each pair can always be referred back to the chosen original undeformed state, we do not claim to have a temporal motion and deformation model beyond two image frames, although we are actively pursuing multi-frame approach [38].

3.4.1. Initial Conditions The integrated motion and deformation analysis framework is formulated such that the mid-wall velocity and the boundary displacements are used as data-based constraints. The unknown field variables are the displacement vectors at the nodal points, although the derivatives of the displacements (velocity and acceleration vectors at the nodal points) can also be derived from the system equations. Since we are only doing frame-to-frame analysis within the time interval T, we assume that the first image frame is sampled at time $t = 0$ and the second image is sampled at time $t = T$. For each pair of image frames at time $t = 0$ and $t = T$, the phase velocity data at $t = 0$ determine the initial conditions of the governing equations, while the shape-based displacements at the boundaries are treated as the boundary conditions of the system which impose prescribed displacements at certain boundary nodal points. Under these two image-based constraints, the integrated motion and deformation recovery can be performed within the finite element framework.

At time $t = 0$, the initial conditions for the system governing equations are as follows:

- The initial displacements of all the points $[\mathbf{U}_{all}(0)]$ are always zero (the object has not moved).
- The three MR phase contrast images provide the three components of the initial velocities $[\dot{\mathbf{U}}_{mid-wall}(0)]$ for the *true* mid-wall points (mid-wall point which are at least one pixel away from the boundaries). For all other points (boundary points and mid-wall points next to the boundaries), we could assume their velocities, $[\dot{\mathbf{U}}_{boundary}(0)]$, to be zero. (This could become a problem because the true mid-wall points and the boundary points now have discontinuity in their velocity values. To avoid this discontinuity problem, we may use the average of true mid-wall velocity values near each boundary point as its initial velocity.)
- The initial accelerations of all the points $[\ddot{\mathbf{U}}_{all}(0)]$ are assumed to be zero.
- The initial equivalent total loads $[R(0)]$ can be computed from the governing equations:

$$\begin{aligned}[R(0)] &= [M][\ddot{\mathbf{U}}_{all}(0)] \\ &+ [C][\dot{\mathbf{U}}_{all}(0)] \\ &+ [K][\mathbf{U}_{all}(0)] \end{aligned} \tag{22}$$

  where $[\dot{\mathbf{U}}_{all}(0)]$ includes both $[\dot{\mathbf{U}}_{mid-wall}(0)]$ and $[\dot{\mathbf{U}}_{boundary}(0)]$.

It should be pointed out that since we will analyze pair-wise motion throughout the cardiac cycle, the estimated velocities and accelerations at time $t = T$ from the previous pair of images can be used as the initial conditions of velocities and accelerations at time $t = 0$ of the current pair of images. However, we must validate these estimates to be accurate before we can trust them. In this paper, we do not use these estimates.

3.4.2. Boundary Conditions From our shape-based boundary motion tracking algorithm, the displacements of some nodal points from $t = 0$ to $t = T$ are known. We note that within the medical imaging domain, several other strategies are also useful for finding displacement information, such as MR tagging [4, 78]. These displacements can be used in our framework with minimal modification. Denoted as $[\mathbf{U}_{boundary}]$, known displacements are used as the boundary conditions of the system at time T. There are a number of ways to apply the boundary conditions to the governing equations. When the boundary conditions are applied, the number of nodal unknowns and the number of equations to be solved are effectively reduced. However, it is most convenient to introduce the known displacements in a way that leaves the original number of equations unchanged and avoids a major restructuring of the system equations [7, 34].

One way to include prescribed nodal displacements while retaining the original structure of system equations is to modify certain diagonal terms of the stiffness matrix $[K]$ and the corresponding terms of the load vector $[R]$. Let the prescribed

International Journal of Computer Vision 35:1, pages 65-85, Nov 1998.

value of the displacement variable U_i (the ith term of the column vector $[\mathbf{U}]$) to be b, the following constraint equation

$$kU_i = kb \tag{23}$$

is added to the system governing equation, with $k \gg K_{ij}$. The modified governing equation for this displacement variable becomes:

$$\begin{aligned} &\sum_{j=1}^{3N} M_{ij}\ddot{U}_j + \sum_{j=1}^{3N} C_{ij}\dot{U}_j + \sum_{j=1}^{3N} K_{ij}U_j + kU_i \\ &= R_i + kb \end{aligned} \tag{24}$$

Therefore, the solution of this modified governing equation must now give

$$U_i \approx b \tag{25}$$

Physically, this procedure can be interpreted as adding a spring of vary large stiffness, and specifying a load which produces the required displacement b for variable U_i. This procedure is repeated until all prescribed displacement variables have been treated. After these modifications have been made, we proceed with the simultaneous solution to the complete set of $3N$ differential equations.

In very strict terms, this modifying procedure will not give the exact values for the prescribed displacements at the corresponding nodal points because we have only modified the $[K]$ and $[R]$ matrices but not the $[M]$ and $[C]$ matrices. In addition, the left side of the ith governing equation includes the sum of the products of the ijth $(j = 1, ..., 3N)$ term of $[K]$ and the j term of $[\mathbf{U}]$. Even though the terms $K_{ij}U_j (j \neq i)$ are small comparing to $K_{ii}U_i$, they still make the solution of the prescribed displacement U_i inexact. However, if the chosen large multiplying factors are indeed very large compared to the values of the matrix terms, the errors will be negligible.

In addition, this inexactness provides a possible method for the incorporation of confidence measures into the displacement boundary conditions. From the discussion in Section 2, we know that the confidence of shape-based point matching between pairs of surfaces can be measured by a metric based upon the *goodness* and *uniqueness* of the match. Since we are using the displacement between these matched points as the prescribed displacements in the unified framework, we treat these displacements differently based on their confidence measures. From this point of view, the large multiplying factor is weighted by the confidence measure for each prescribed displacement. The displacements with high confidence measures have *really large* multiplying factors to enforce the system solution to give the exact prescribed values at these nodal points, while the displacements with low confidence measures would have relatively small multiplying factors to have inexact solution values, which are the compromise of the prescribed conditions and the smoothness constraint which is implicitly enforced by the constitutive laws of the materials.

3.4.3. Numerical Solution After setting up the initial and displacement boundary conditions, the finite element system is regarded as an elastic object in static conditions when some outside loads are applied to certain nodal points. Therefore, the object moves and deforms because of these forces. Mathematically, the governing equations represent a system of differential equations of second order and, in principle, the solution to the equations can be obtained by standard procedures for the solution of differential equations with constant coefficients. However, the procedure proposed for the solution of general systems of differential equations can become very expensive if the order of the matrices is large. In practice, these types of systems are almost always solved by numerical means.

In direct integration, the governing equations are integrated using a numerical step-by-step procedure. Instead of trying to satisfy Equation 21 at any time t, it is aimed to satisfy the governing equations only at discrete time intervals Δt apart. This means that equilibrium, which includes the effects of inertia and damping forces, is sought at discrete time points within the interval of solution. In addition, a variation of displacements, velocities, and accelerations within each time interval is assumed. It is the form of assumption on the variation that determines the accuracy, stability, and the cost of the solution procedure [7]. We have chosen the Newmark method, which is unconditionally stable, to solve the equations.

One additional step is applied to make the integration process more stable and accurate. To reduce the oscillation of the elastic body of the left ventricle, the displacement boundary conditions

International Journal of Computer Vision 35:1, pages 65-85, Nov 1998.

are enforced gradually. If there are n integration steps between $t = 0$ and $t = T$, the enforced displacement U_i^k at step k of the integration is:

$$U_i^k = U_i sin\left(\frac{\pi}{2}\frac{k}{n}\right) \tag{26}$$

where U_i is the prescribed displacement at T. By enforcing the prescribed displacements this way, the elastic object makes larger movement at the beginning of the integration, and it moves less towards the end of the time interval. Hence, the system is more stable when it reaches time $t = T$.

The numerical solution obtained from the integration of the governing equations produces the estimated displacements, velocities, and accelerations of the left ventricle at time $t = T$, the end time of the pair of image frames. These motion estimates are derived from an integrated framework which is based on a linear elastic mechanical model of the myocardium, and is constrained by the initial velocity information from the MR phase images and the shape-based boundary displacements. It takes advantage of the complementary nature of these image sources, and uses the material constitutive relationships to produce a mechanically plausible solution to the system governing equations. It should be pointed out that the motion analysis can be done for every pair of the images throughout the cardiac cycle. If the global coordinate systems are the same for all pairwise operations, the displacements at any time frame can always be referred to the chosen initial state, usually the end of diastole. After the displacements have been calculated, the coordinate-dependent strain tensor ϵ for each tetrahedral element can be computed. Furthermore, the principal strain tensor ϵ_p of each tetrahedral element can also be computed as the eigenvalues and eigenvectors of the tensor ϵ.

In principle, using the finite element framework to track motion between temporal images can be regarded as a predictor from time $t = 0$ to time $t = T$. Since we already have data information at $t = T$ in terms of the segmented endocardial and epicardial surfaces, as well as the mid-wall velocities, we can refine the motion estimate between $t = 0$ and $t = T$ by comparing how close the image-driven, model-based prediction comes to the actual data. The differences between the data and the prediction can be used as a recursive feedback term to improve the matching process. Initial work regarding this feedback process in two-dimensional case has been reported [58].

4. Experimental Results

The integrated motion and deformation analysis framework proposed has been implemented. Experiments have been conducted with real cardiac MR phase contrast images from a normal canine study.

Figure 5 shows an example of phase contrast images of a canine study. In this dataset, three contiguous short axis slices were collected using the cine phase contrast gradient echo sequence for sixteen time frames. The imaging parameters were: flip angle = 30°, $TE = 34msec$, $TR = 34msec$, $FOV = 28cm$, $5mm$ skip 0, matrix 256x128, 4 nex, venc = $15cm/sec$. The in-plane resolution of the dataset is $1.09mm/pixel$, and the interplane resolution is $5mm$. The intensity values of the velocity images range from $-150mm/sec$ to $150mm/sec$, with the signs of the value indicating the directions of the velocities. The dog was infarcted to cause dyskinetic motion at the inter-ventricular septum (the lower left part of the LV). Again, it is important to notice that the magnitude image and the three directional velocity images are perfectly registered since they are acquired from the same complex MR signal. It should also be noted that because of the time (ten to fifteen minutes) to acquire each set of directional phase velocity images (three slices are acquired at each time), the image dataset only covers a small part of the left ventricle. However, this does not alter the validity of using this dataset to test the capability of the integrated framework except that there is 3D motion out of the field of view vertically.

Since it is more desirable to have roughly equal resolutions in all three dimensions to track surface motion, interpolation is needed between the data contour slices. A chamfer distance based contour interpolation is used to insert three interpolated contours to every two consecutive data contours. Figure 6 shows the bending energy maps and the wireframes of the interpolated endocardial and epicardial surface at end diastole. The shape-based surface motion tracking process is

International Journal of Computer Vision 35:1, pages 65-85, Nov 1998.

then applied to the sixteen interpolated surface sequences, once for the endocardium and once for the epicardium. This way, the surface displacements have $1.09mm$ in-plane resolution and $1.25mm$ inter-plane resolution. A subset of the surface point displacements (ten percent) are used as the boundary displacement constraints in the integrated volumetric framework.

The velocity images currently have $5mm$ inter-plane resolution. To handle this relatively lower resolution, we have either inserted three trilinearly interpolated velocity images into every two data velocity images, or for computational reasons, we have coarsely re-sampled the in-plane images to reduce the in-plane resolution to $4.36mm$. In the example given in this section, the velocity images are re-sampled to lower resolution to save computation time. The mid-wall velocities of the phase contrast images are used as the initial velocity constraints in the integrated volumetric framework. The myocardial surfaces are also re-sampled to the same lower resolutions of $4.36mm/pixel$ in-plane and $5mm/pixel$ inter-plane after the surface motion tracking has been performed. This way, even though the final re-sampled dataset has only $4.36mm$ in-plane and $5mm$ inter-plane resolutions to form larger tetrahedral elements to save computational expense, the boundary displacements still have $1.09mm$ in-plane and $1.25mm$ inter-plane resolutions. The myocardial sample points which are bounded by the endocardial and epicardial boundaries are Delaunay tessellated to form the finite element mesh of the myocardium. Figure 7 shows the low resolution tetrahedral finite element mesh of the mid-ventricle covered by the three-slice image set. In this case, there are 2147 tetrahedra in the mesh.

After the boundary displacement tracking process, the velocity image re-sampling process, and the finite element mesh construction process, we can now perform the integrated volumetric motion and deformation analysis. Following the procedures established in the previous sections, the governing equations of the myocardium are derived from the minimum potential energy principle. A linear isotropic elastic myocardial model is used, and the material-related constants that have been established experimentally for the myocardium in the biomechanics literature [76] are used, with Young's modulus set to be $75,000Pascal$, Poisson's ratio set to around 0.5, the myocardial mass density set to $1.5g/mm^3$, and the damping parameter set to under 0.1. The velocity values at the mid-wall points are used as the initial velocity conditions, and the surface displacements are used as the displacement boundary conditions. Since the temporal resolution of the dataset is $0.03125sec/frame$, we choose the integration time step $\Delta t = 0.003125sec$ to have 10 integrated steps. Using these constraints and parameters, the motion and deformation parameters of the myocardium at all sixteen time frames are calculated using the Newmark integration process. In the experiment shown here, there are 2147 tetrahedra in the finite element mesh. The required computer memory for the system to handle this data set is around 60MB. The computation time for each pair of images is about half hours on a Silicon Graphics HighImpact workstation with 195 MHZ R10000 processor and 128MB memory.

Figure 8 presents the two-dimensional projection of the three-dimensional dense field displacement vector map of the middle slice from ED to the next time frame, found from the integrated framework. The use of 2D projections instead of a true 3D vector map is only because of the ease of visualization. Here, a vector arrow begins from its position at present time (ED), and ends at its position in the next time frame. The non-homogeneous nature of the myocardial motion is very evident from this displacement map: different regions of the myocardium display very different motion characteristics in direction and magnitude.

While the displacements or path lengths of the myocardial points are useful for predicting the state of health of the left ventricle, the element strain tensors of the myocardial tissues provide the non-homogeneous deformation information among regions which could be used to quantify transmural function, especially issues related to the extent of myocardial injury [26]. Even though we believe more detailed and sophisticated analysis on a range of image datasets under different physiological conditions is required to infer any useful information for clinical and research purposes, we still proceed to compute the strain measures on this particular dataset to test the capability of our integrated framework. To that end, we have calculated the strain tensors for each

International Journal of Computer Vision 35:1, pages 65-85, Nov 1998.

tetrahedral element of the finite element grid to depict the non-rigid deformation, excluding the rigid bulk motion of the elements. Figure 9 shows the three normal components (xx, yy, and zz components) and three shear components (xy, yz and zx components) of the strain tensor for the deformation between ED and ES. It seems that these three slices of mid-ventricle myocardium undergo very little z direction deformation. The large strain at lower left part of the LV may be explained by the dyskinetic motion caused by the infarction (we want to emphasize that this is a very intuitive explanation for these strain maps, there should be no conclusion drawn from this initial experiment). Figure 10 shows the more object-centered principal strain maps of the same deformation: the three principal components of the strain as well as the two-dimensional projections of the three-dimensional dense directions of the maximum principal strain (middle slice). Once again, large strain is observed at the lower left part of the LV. In both Figure 9 and 10, the strain values are mapped back to the myocardial grid at its original state (ED). In these figures, the negative strain values (contraction) are represent by different shades of blue, and the positive values (expansion) are represent by different shades of red. Also, we want to point out that the apparent non-uniform strains transmurally across the heart wall, which could be extremely important in validating the clinical hypothesis that the ischemic disease progresses transmurally overtime. Of cause, any significant claim can only be made after more carefully designed validation on a range of image datasets. Figure 11 shows a cutaway view of the maximal principal strain map at ES with respect to ED. In addition, we are currently looking into the possibility of calculating strains in the myofiber directions which have been documented [36]. This way, it can not only more accurately and meaningfully compute and interpret the strain information, it can also facilitate the future plan of including active myocardial tension development.

The temporal changes of the strain tensors are investigated and compared to earlier observations available from biomechanics and cardiology literature [50, 72]. Since we have only three mid-ventricle image slices, it is difficult to reliably define the radial, longitudinal, and circumferential directions and the associated strain measures in those directions which are commonly used in the cardiology community. Instead, the temporal changes of the object-centered principal strains are compared to the data from literature. Previously, the available principal strain data are often observed at isolated positions of the myocardium varying from study to study. Here, we compare the average values of strains of all the elements to these isolated strain data. In the literature [50, 72], the values of the first (maximum) principal strain has been observed to reach a maximum strain of 30% to 40% at ES, the second principal strain has very small values, and the third (minimum) principal strain reaches an extreme value of -20% at ES. For our experiment, we observe that the average value of the first principal strain reaches a maximum strain of 32% at ES, the average second strain is very small and stable, and the third principal strain reaches -18% at ES. Obviously, these results are quite consistent with previous studies. However, we should point out that our integrated motion and deformation framework can noninvasively obtain the *dense motion and strain fields* instead of only finding these information at isolated positions, as was done previously. In addition, the framework's ability to quantify the difference of motion and deformation characteristics between myocardial tissue elements makes it valuable to evaluate cardiac regional function. Figure 12 shows the temporal sequence of the first principal strain maps from ED to ES. Note the different strain values between different regions.

We want to point out that although the proposed framework is intended to integrate complementary image constraints within a unified system, it also can be used for motion and deformation analysis using only one image source. The uniqueness of this framework is that it can take single or multiple image based data constraints, often very noisy by themselves, and estimate the best compromise motion and deformation parameters from these data and the mechanical model of the left ventricle, which provides a natural way to enforce the physically plausible potential energy functional and smoothness constraints. Further, the actual physical constraints related to known cardiac parameters such as pressure can also be incorporated into the system as external loads.

International Journal of Computer Vision 35:1, pages 65-85, Nov 1998.

5. Conclusions

We have developed an integrated framework for the analysis of left ventricular motion and deformation. This unified approach is based upon the use of image analysis strategies and mechanical modeling of the myocardium, and is embedded in a finite element framework for the integration of complementary image sources.

This integrated motion and deformation analysis framework estimates the optimal motion and deformation parameters from noisy and complementary image data. Image-derived information from myocardial surfaces and the mid-wall are used in locations where they have the best signals. These data constraints are used as the initial and boundary conditions in the system governing equations of the finite element framework. A continuum mechanical model of the myocardium is applied to provide physically meaningful constraints on the dynamic behaviors of the LV tissue. Experiments have been performed on canine MR phase contrast images. Motion and deformation parameters are estimated from the integration of boundary displacement information and mid-wall phase velocity information. Results have been compared to previous studies in the literature.

Ongoing and future work includes adopting more sophisticated continuum biomechanical models of the myocardium based on the theory of finite deformation. Temporal periodic characteristics of the heart motion as well as 3D feedback mechanism will also be incorporated into the current framework. Data from sixteen canine experiments are being complied for testing and validation over the next one and half years.

While the framework presented here is aimed at cardiac function analysis, some aspects of it should have more applications in certain areas of computer vision research in general. The use of true physical models of the objects enables us to incorporate more meaningful constraints, and the integration of complementary image-derived sources will help achieve more robust results from noisy data.

References

1. A. A. Amini and J. S. Duncan. Bending and stretching models for LV wall motion analysis from curves and surfaces. *Image and Vision Computing*, 10(6):418–430, 1992.
2. A.A. Amini, Y.S. Chen, R.W. Curwen, V. Mani, and J. Sun. Coupled b-snake grids and constrained thin-plate splines for analysis of 2-d tissue deformations from tagged mri. *IEEE Transactions on Medical Imaging*, 17(3):344–356, June 1998.
3. P. Anandan. A computational framework and an algorithm for the measurement of visual motion. *International Journal of Computer Vision*, 2:283–310, 1989.
4. L. Axel and L. Dougherty. MR imaging of motion with spatial modulation of magnetization. *Radiology*, 171:841–845, 1989.
5. Azhari et al. Noninvasive quantification of principal strains in normal canine hearts using tagged MRI images in 3D. *American Journal of Physiology*, 264:H205–H216, 1993.
6. R.K. Bajcsy and C. Broit. Matching of deformed images. In *International Conference on Pattern Recognition*, pages 351–353, 1982.
7. K. Bathe and E. Wilson. *Numerical Methods in Finite Element Analysis*. Prentice-Hall, New Jersey, 1976.
8. R. Battiti, E. Amaldi, and C. Koch. Computing optical flow across multiple scales: An adaptive coarse-to-fine strategy. *International Journal of Computer Vision*, 6(2):133–145, June 1991.
9. M.J. Black and Y. Yacoob. Recognizing facial expressions in image sequences using local parameterized models of image motion. *International Journal of Computer Vision*, 25(1):23–48, October 1997.
10. E. L. Bolson, S. Kliman, F. Sheehan, and H. T. Dodge. Left ventricular segmental wall motion - A new method using local direction information. In *Proceedings of Computers in Cardiology*, 1980.
11. F. L. Bookstein. Principal warps: Thin-plate splines and the decomposition of deformations. *IEEE Transactions on Pattern Analysis and Machine Intelligence*, pages 567–585, 1989.
12. A. Chakraborty and J.S. Duncan. Game-theoretic integration for image segmentation. *IEEE Transactions on Pattern Analysis and Machine Intelligence*, 21(1):12–30, January 1999.

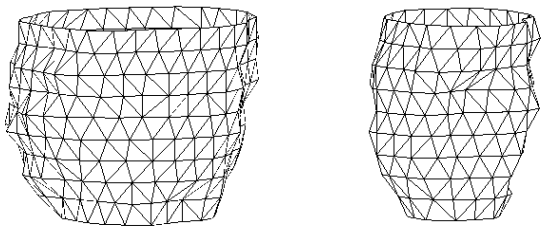

Fig. 1. Delaunay triangulation of myocardial surfaces: epicardial (left), endocardial(right).

International Journal of Computer Vision 35:1, pages 65-85, Nov 1998.

13. J. Chesebro, G. Knatterrud, and others. Thrombolysis in myocardial infarction (TIMI) trial phase I: A comparison between intravenous tissue plasminogen activator and intravenous streptokinase. *Circulation*, 76:142–154, 1987.
14. R.T. Constable, K. Rath, A. Sinusas, and J. Gore. Development and evaluation of tracking algorithms for cardiac wall motion analysis using phase velocity MR imaging. *Magnetic Resonance in Medicine*, 32:33–42, 1994.
15. N. Cornelius and T. Kanade. Adapting optical-flow to measure object motion in reflectance and x-ray image sequences. In *DARPA Image Understanding Workshop*, pages 257–265, 1983.
16. J.L. Crowley and A.C. Sanderson. Multiple resolution representation and probabilistic matching of 2-d gray-scale shape. *IEEE Transactions on Pattern Analysis and Machine Intelligence*, 9(1):113–121, January 1987.
17. D. DeCarlo and D. Metaxas. Blended deformable models. *IEEE Transactions on Pattern Analysis and Machine Intelligence*, 18(4):443–448, April 1996.
18. T. Denney and J. L. Prince. 3D displacement field reconstruction from planar tagged cardiac MR images. In *Proceedings of the IEEE Workshop on Biomedical Image Analysis*, pages 51–60, 1994.
19. M. P. do Carmo. *Differential Geometry of Curves and Surfaces*. Prentice-Hall, New Jersey, 1976.
20. I. A. Essa and A. P. Pentland. Coding, analysis, interpretation, and recognition of facial expressions. *IEEE Transactions on Pattern Analysis and Machine Intelligence*, 19(7):757–763, 1997.
21. O. Faugeras. *Three-dimensional Computer Vision: A Geometric Viewpoint*. MIT Press, 1993.
22. Y. C. Fung. *A First Course in Continuum Mechanics*. Prentice-Hall, 1977.

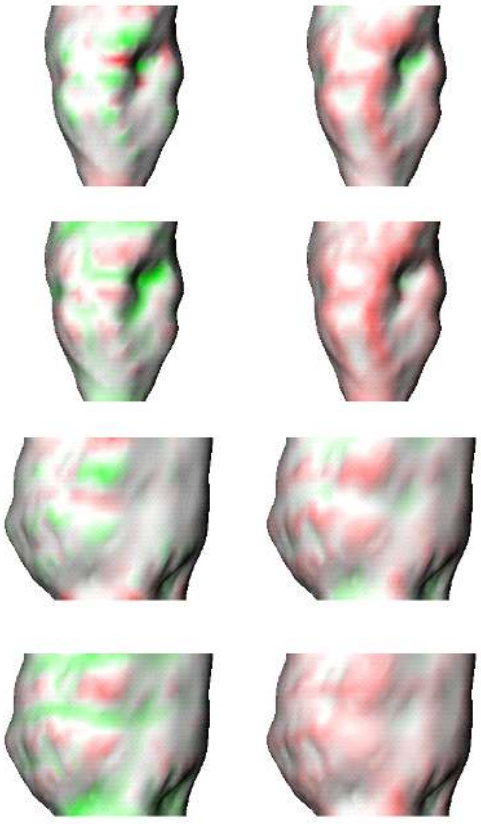

Fig. 2. Curvature maps of myocardial surfaces. Top two rows: Gaussian, mean, maximum principal, minimum principal curvature maps of one endocardial surface at one time point; Bottom two rows: Gaussian, mean, maximum principal, minimum principal curvature maps of one epicardial surface at the same time point. (Green: positive curvature values; Red: negative curvature values.)

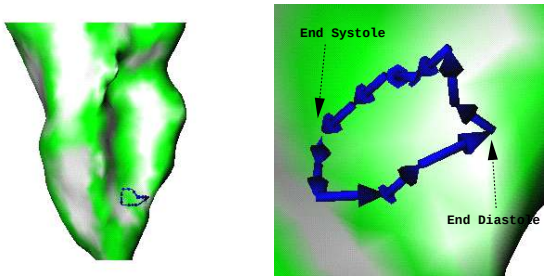

Fig. 3. Shape-tracked complete trajectory of an endocardial point over the cardiac cycle, superimposed onto the endocardial surface at end systole: overview (left), detail (right).

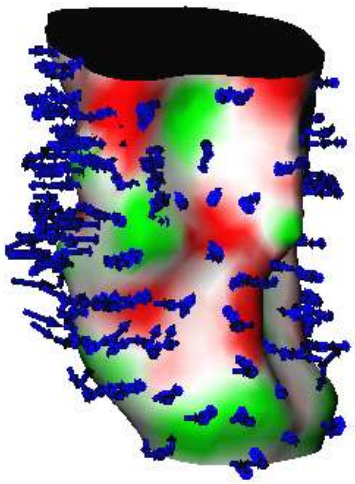

Fig. 4. Shape-tracked dense endocardial displacement vector field of a MRI dataset from ED to ES, sub-sampled for visualization purposes. The trajectories are shown against the rendered endocardial Gaussian curvature map at ES.

23. H. Gelberg, B. Brundage, S. Glantz, and W. Parmley. Quantitative left ventricular wall motion analysis: A comparison of area, chord and radial methods. *Circulation*, 59(5):991–1000, 1979.
24. D. Gibson, T. Prewitt, and D. Brown. Analysis of left ventricular wall movement during isovolumic relaxation and its relation to coronary artery disease. *British Heart Journal*, 38:1010, 1976.
25. L. Goncalves, E. Di Bernardo, E. Ursella, and P. Perona. Monocular tracking of the human arm in 3D. In *Fifth International Conference on Computer Vision*, pages 764–770, 1995.
26. W. Grossman. Assessment of regional myocardial function. *Journal of American College of Cardiology*, 7(2):327–328, 1986.
27. J. M. Guccione, A. D. McCulloch, and L. K. Waldman. Passive material properties of intact ventricular myocardium determined from a cylindrical model. *Journal of Biomechanical Engineering*, 113:42–55, 1991.
28. R. J. Herfkens, N. J. Pelc, L. R. Pelc, and J. Sayre. Right ventricular strain measured by phase contrast MRI. In *Proceedings of the 10th Annual Society of Magnetic Resonance Medicine*, page 163, San Francisco, 1991.
29. E. C. Hildreth. *The Measurement of Visual Motion*. MIT Press, Cambridge, 1984.
30. H. Honda, Y. Koiwa, K. Takagi, J. Kikuchi, N. Hoshi, T. Takishima, and J. P. Butler. Noninvasive measurement of left ventricular myocardial elasticity. *American Journal of Physiology*, pages H881–H890, 1994.
31. B. K. P. Horn. *Robot Vision*. MIT Press, Cambridge, 1986.
32. B. K. P. Horn and B. G. Schunck. Determining optical flow. *Artificial Intelligence*, 17:185–203, 1981.
33. B. Horowitz and S. Pentland. Recovery of non- rigid motion and structure. In *Proceedings of the IEEE Conference on Computer Vision and Pattern Recognition*, pages 325–330, Maui, June 1991.
34. K. H. Huebner, E. A. Thornton, and T. G. Byrom. *The Finite Element Method For Engineers*. John Wiley & Sons, New York, 1995.

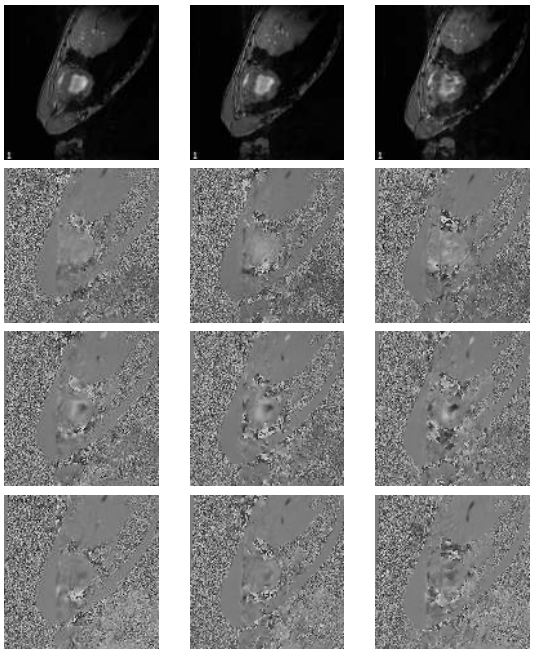

Fig. 5. 3D MR phase contrast images at ED. First row: the magnitude images from lower-most to upper-most slice; Second row: x dimension velocity images; Third row: y dimension velocity images; Fourth row: z dimension velocity images.

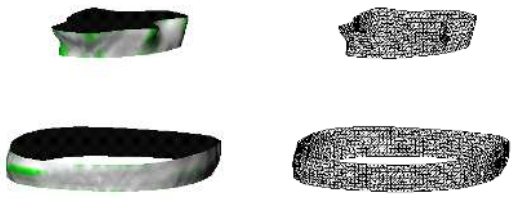

Fig. 6. Myocardial Surfaces derived from phase contrast MR images. Top left: the endocardial potential energy map (more green indicates higher energy); Top right: the endocardial surface wireframe; Bottom left: the epicardial potential energy map; Bottom right: the endocardial surface wireframe.

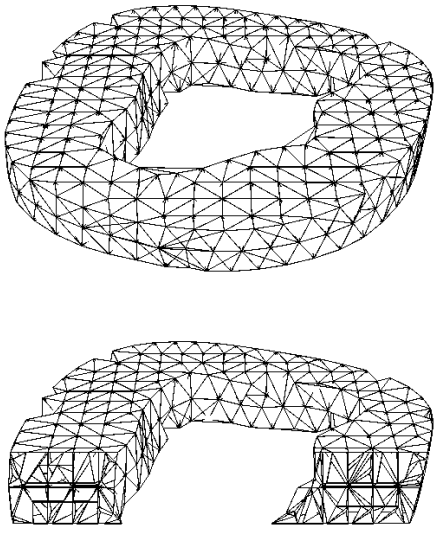

Fig. 7. Volumetric finite element mesh of the midventricle from phase contrast MR images. Top: overall view; Bottom: cutaway view.

International Journal of Computer Vision 35:1, pages 65-85, Nov 1998.

35. J. D. Humphrey and F. C. P. Yin. Biomechanical experiments on excised myocardium: theoretical considerations. *Journal of Biomechanics*, 22:377–383, 1990.

36. P. J. Hunter, P. M. F. Nielsen, B. H. Smaill, and I. J. LeGrice. An anatomical heart model with applications to myocardial activation and ventricular mechanics. *Critical Reviews in Biomedical Engineering*, 20:403–426, 1992.

37. P. J. Hunter and B. H. Smaill. The analysis of cardiac function: a continuum approach. *Progress in Biophysics and Molecular Biology*, 52:101–164, 1989.

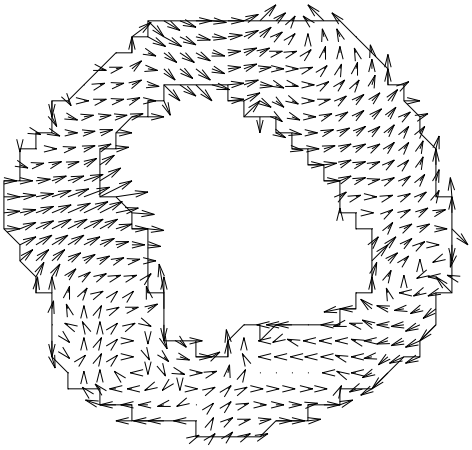

Fig. 8. Dense field displacement vector map (2D projection) from the integrated framework. Note the non-homogeneous nature of the myocardial motion.

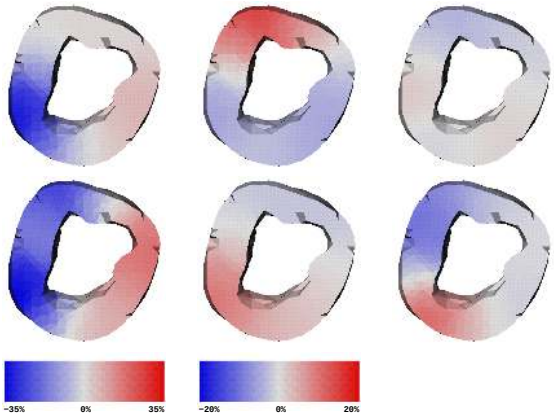

Fig. 9. 3D strain maps of mid-ventricle (ED-ES). Top left: x-direction normal strain; Top middle: y-direction normal strain; Top right: z-direction normal strain; Middle left: xy-direction shear strain; Middle middle: yz-direction shear strain; Middle right: zx-direction shear strain; Bottom left: color scale for x-direction normal strain; Bottom middle: color scale for all other strains.

38. J. C. McEachen II and J. S. Duncan. Shape-based tracking of left ventricular wall motion. *IEEE Transactions on Medical Imaging*, 16(3):270–283, 1997.

39. C. Kambhamettu and D.B. Goldgof. Curvature-based approach to point correspondence recovery in conformal nonrigid motion. *CVGIP: Image Understanding*, 60(1):26–43, July 1994.

40. G. E. Mailloux, A. Bleau, M. Bertrand, and R. Petitclerc. Computer analysis of heart motion from two dimensional echocardiograms. *IEEE Transactions on Biomedical Engineering*, BME-34(5):356–364, May 1987.

41. D. Marr. *Vision*. W. H. Freeman and Co., 1982.

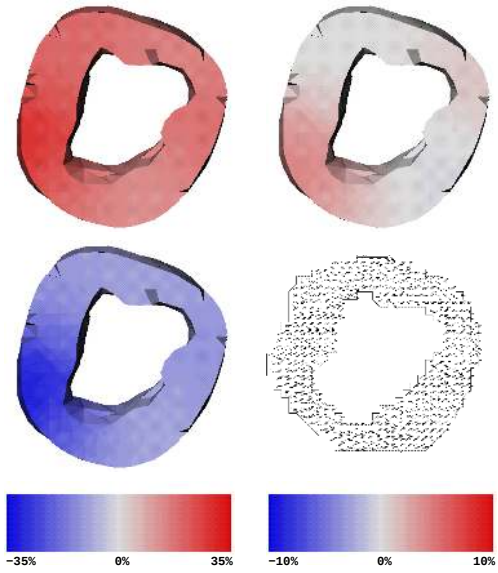

Fig. 10. 3D principal strain maps of mid-ventricle (ED-ES). Top left: the first (maximum) principal strain; Top right: the second principal strain; Middle left: the third (minimum) principal strain; Middle right: two-dimensional projections of the three-dimensional directions of the maximum principal strain (middle slice). Bottom left: color scale for the first and third principal strains; Bottom right: color scale for the second principal strains.

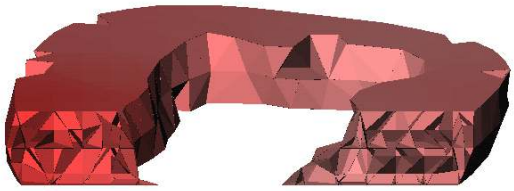

Fig. 11. Cutaway view of the maximal principal strain map at ES with respect to ED.

42. A. McCulloch, L. Waldman, J. Rogers, and J. Guccione. Large-scale finite element analysis of the beating heart. *Critical Reviews in Biomedical Engineering*, 20:427–449, 1992.
43. F. G. Meyer, R. T. Constable, A. J. Sinusas, and J. S. Duncan. Tracking myocardial deformation using spatially constrained velocities. *IEEE Transactions on Medical Imaging*, 15(4):453–465, 1996.
44. H. H. Nagel and W. Enkelmann. An investigation of smoothness constraints for the estimation of displacement vector fields from image sequences. *IEEE Transactions on Pattern Analysis and Machine Intelligence*, 8:565–593, 1986.
45. C. Nastar and N. Ayache. Frequency-based nonrigid motion analysis: Application to four dimensional medical images. *IEEE Transactions on Pattern Analysis and Machine Intelligence*, 18(11):1067–1079, November 1996.
46. G. Nayler, N. Firmin, and D. Longmore. Blood flow imaging by cine magnetic resonance. *Journal of Computer Assisted Tomography*, 10:715–722, 1986.
47. S. A. Niyogi and E. H. Adelson. Analyzing gait with spatiotemporal surfaces. In *Proceedings of the workshop on motion of non-rigid and articulated bodies*, pages 16–24, November 1994.
48. V. P. Novak, F. C. P. Yin, and J. D. Humphrey. Regional mechanical properties of passive myocardium. *Journal of Biomechanics*, 27(4):403–412, 1994.
49. W.G. O'Dell, C.C. Moore, W. Hunter, E.A. Zerhouni, and E.R. McVeigh. Displacement field fitting for calculating 3D myocardial deformations from tagged MR images. *Radiology*, 195:829–835, 1995.
50. J. H. Omens, D. A. MacKenna, and A. D. McCulloch. Measurement of strain and analysis of stress in resting rat left ventricular myocardium. *Journal of Biomechanics*, 26(6):665–676, 1993.
51. R. Owen, L. Staib, P. Anandan, and J. Duncan. Measurement of non-rigid motion in images using contour shape descriptors. In *Proceedings of the IEEE Conference on Computer Vision and Pattern Recognition*, 1991.
52. K. Palaniappa, C. Kambhamettu, A. F. Hasler, and D. B. Goldgof. Structure and semi-fluid motion analysis of stereoscopic satellite images for cloud tracking. In *Fifth International Conference on Computer Vision*, pages 659–665, 1995.
53. X. Papademetris, P. Shi, D.P. Dione, A.J. Sinusas, R.T. Constable, and J.S. Duncan. Recovery of soft tissue object deformation from 3d image sequences using biomechanical models. In *Information processing in medical imaging*, page in press, 1999.
54. J. Park, D. Metaxas, and L. Axel. Volumetric deformable models with parameter functions: a new approach to the 3D motion analysis of the LV from MRI-SPAMM. In *Fifth International Conference on Computer Vision*, pages 700–705, 1995.
55. N. J. Pelc, R. J. Herfkens, and L. R. Pelc. 3D analysis of myocardial motion and deformation with phase contrast cine MRI. In *Proceedings of the 11th Annual Society of Magnatic Resonance Medicine*, page 18, Berlin, 1992.
56. N. J. Pelc, R. J. Herfkens, A. Shimakawa, and D. Enzmann. Phase contrast cine magnetic resonance imaging. *Magnetic Resonance Quarterly*, 7(4):229–254, 1991.
57. S. Sclaroff and A. P. Pentland. Modal matching for correspondence and recognition. *IEEE Transactions on Pattern Analysis and Machine Intelligence*, 17(6):545–561, 1995.
58. P. Shi, G. Robinson, R. T. Constable, A. Sinusas, and J. Duncan. A model-based integrated approach to track myocardial deformation using displacement and velocity constraints. In *Fifth International Conference on Computer Vision*, pages 687–692, 1995.
59. P. Shi, A. Sinusas, R. T. Constable, E. Ritman, and J. Duncan. Point-tracked quantitative analysis of left ventricular motion from 3d image sequences. *IEEE Transactions on Medical Imaging*, in press, 1999.
60. Pengcheng Shi. *Image Analysis of 3D Cardiac Motion Using Physical and Geometrical Models*. PhD thesis, Yale University, New Haven, CT, 1996.
61. C. Slager, T. Hooghoudt, P. Serruys, J. Schuurbiers, and J. Reiber et al. Quantitative assessment of regional left ventricular motion using endocardial landmarks. *Journal of American College of Cardiology*, 7(2):317–326, 1986.
62. B. H. Smaill and P. J. Hunter. Structure and function of the diastolic heart: material properties of the passive myocardium. In *Theory of the heart*, Berlin, 1991. Springer-Verlag.
63. S. Song and R. Leahy. Computation of 3D velocity fields from 3D cine CT images. *IEEE Transactions on Medical Imaging*, 10:295–306, Sept 1991.
64. A. Spencer. *Continuum Mechanics*. Longman, London, 1980.
65. L. Staib and J. S. Duncan. Parametrically deformable contour models. *IEEE Transactions on Pattern Analysis and Machine Intelligence*, 14(11):1061–1075, 1992.
66. G. Taubin. Curve and surface smoothing without shrinkage. In *Proceedings of the Fifth International Conference on Computer Vision*, pages 852–857, 1995.

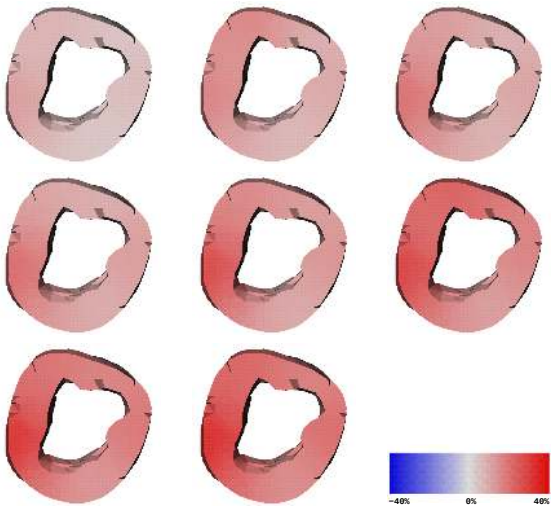

Fig. 12. Temporal maps of the first principal strain (ED-ES) from phase contrast MR images.

International Journal of Computer Vision 35:1, pages 65-85, Nov 1998.

67. D. Terzopoulos and D. Metaxas. Dynamic 3D models with local and global deformation: Deformable superquadrics. *IEEE Transactions on Pattern Analysis and Machine Intelligence*, 13(17), 1991.
68. D. Terzopoulos and M. Vasilescu. Sampling and reconstruction with adaptive meshes. In *Proceedings of the IEEE Conference on Computer Vision and Pattern Recognition*, pages 70–75, 1991.
69. M. Tistarelli and G. Marcenaro. Using optical flow to analyze the motion of human body organs from bioimages. In *Proceedings of the IEEE Workshop on Biomedical Image Analysis*, pages 100–109, 1994.
70. J.K. Tsotsos, J. Mylopoulos, H.D. Covvey, and S.W. Zucker. A framework for visual motion understanding. *IEEE Transactions on Pattern Analysis and Machine Intelligence*, 2(6):563–573, November 1980.
71. S. Ullman. *The Interpretation of Visual Motion*. MIT Press, Cambridge, 1979.
72. L. K. Waldman, Y. C. Fung, and J. W. Covell. Transmural myocardial deformation in the canine left ventricle: normal in vivo three–dimensional finite strains. *Circulation Research*, 57:152–163, 1985.
73. D. F. Watson. Computing the n-dimensional delaunay tessellation with application to Voronoi polytopes. *The Computer Journal*, 24:167–172, 1981.
74. V. Wedeen. Magnetic resonance imaging of myocardial kinematics: technique to detect, localize and quantify the strain rates of active human myocardium. *Magnetic Resonance Medicine*, 27:52–67, 1992.
75. Y. Xiong and S.A. Shafer. Hypergeometric filters for optical flow and affine matching. *International Journal of Computer Vision*, 24(2):163–177, September 1997.
76. H. Yamada. *Strength of Biological Material*. The Williams and Wilkins Company, Baltimore, 1970.
77. A. A. Young, L. Axel, L. Dougherty, D. Bogen, and C. Parenteau. Validation of MRI tagging to estimate material deformation. *Radiology*, 188:101–108, 1993.
78. E. Zerhouni et al. Tagging of the human heart by multiplanar selective RF saturation for the analysis of myocardial contraction. In *Abstracts of the Annual Meeting of the Society of Magnetic Resonance in Imaging*, page 10, San Francisco, 1988.

Pengcheng Shi is an assistant professor of computer and information science at the New Jersey Institute of Technology. His research interests include visual information processing, especially its biomedical applications, computational geometry, and biological system modeling. His work on computer vision and image analysis began while he was with the Image Processing and Analysis Group (IPAG) at Yale University, where he received his PhD degree.

Albert J. Sinusas is an associate professor of cardiology and diagnostic radiology at Yale University School of Medicine. He has focused on the development of non-invasive 3D multi-modality imaging approaches (MRI, SPECT, PET) for the assessment of myocardial viability, and the evaluation of the interrelationship of myocardial perfusion, metabolism, and function.

R. Todd Constable is an assistant professor of diagnostic radiology at Yale University School of Medicine. He has been conducting research on the development of magnetic resonance imaging techniques to provide high quality images of anatomical and functional information of the brain and the heart.

James S. Duncan is professor of electrical engineering and diagnostic radiology, and director of the Image Processing and Analysis Group (IPAG) at Yale University. His research focuses on the use of geometrically and physically-based models in conjunction with mathematical optimization strategies to recover structural and functional information from medical and biological images.